Materials Today Physics 7 (2018) 77–88

Contents lists available at ScienceDirect

Materials Today Physics

journal homepage: https://www.journals.elsevier.com/materials-today-physics

Investigations on electrical and thermal transport properties of Cu_2SnSe_3 with unusual coexisting nanophases

Y. Zhou [a, 1], H. Wu [b, 1], D. Wang [a, 1], L. Fu [c], Y. Zhang [b], J. He [c], S.J. Pennycook [b, **], L.-D. Zhao [a, *]

[a] School of Materials Science and Engineering, Beihang University, Beijing 100191, China
[b] Department of Materials Science and Engineering, National University of Singapore, 7 Engineering Drive 1, Singapore 117575, Singapore
[c] Department of Physics, South University of Science and Technology of China, Shenzhen 518055, China

ARTICLE INFO

Article history:
Received 28 October 2018
Received in revised form
5 November 2018
Accepted 6 November 2018

Keywords:
Thermoelectric
Diamond-like compound
Cu_2SnSe_3
Phase coexistence

ABSTRACT

The ternary diamond-like compound Cu_2SnSe_3 is a potential thermoelectric material. Its Cu-Se conducting network leaves Sn as a likely doping site to optimize the carrier concentration without much deterioration to the carrier mobility. Thus, the precise determination on the intricate phase structures of Cu_2SnSe_3 is critical. Here, we first use the atomically resolved scanning transmission electron microscopy and reveal an unusual phase coexistence (monoclinic and orthorhombic phases) in Ag-doped Cu_2SnSe_3. Owing to coexisting phases and the order–disorder transition in the orthorhombic phase, the Ag-doped Cu_2SnSe_3 shows an unusual three-stage behavior in its temperature-dependent electrical transport properties and achieves record high power factors in this system. The observed three-stage behavior due to the phase coexistence is supported by the first principle calculations, Hall measurements, and optical diffuse reflectance measurements. To fully understand the band structures and the coherent interface between these coexisting phases, a band contact model is proposed that could well explain the three-stage electrical transport behavior. Moreover, the phase coexistence is observed at the nanoscale regime, thus providing a high density of phase boundaries. Such coexisting nanophases play an important role in lowering the lattice thermal conductivity. As a result, the *ZT* value obtained in $Cu_2Sn_{0.93}Ag_{0.07}Se_3$ is double that of undoped Cu_2SnSe_3.

Introduction

In the past few decades, the energy crisis has fueled the demand for new energy sources along with more efficient energy utilization. Thermoelectric (TE) materials, which can directly convert waste heat to electricity, provide an alternative option for optimizing the energy utilization process. The power conversion efficiency of a TE material is characterized by the dimensionless figure of merit (*ZT*), defined by $ZT = S\sigma^2T/\kappa$, where *S*, σ, κ, and *T* are the Seebeck coefficient, electrical conductivity, thermal conductivity, and working temperature in Kelvin, respectively. Judging only by the equation, a high *ZT* value can be achieved in a system having both a high power factor (PF, produced by $S\sigma^2$) and a low thermal conductivity. However, the intricate interactions of these TE parameters make it difficult to simultaneously meet these requirements. A criterion has been proposed as 'phonon-glass-electron-crystal' for high *ZT* candidates, which requires specific structures to allow the coexistence of the different transport channels for electrons and phonons in one given material. Obeying this criterion, diverse mechanisms have been adopted to enhance the *ZT* values of different material systems in recent years, such as enhancing the electrical transport properties through band structure engineering [1–3,67] and lowering lattice thermal conductivity by nanostructuring [4–7]. Remarkable improvements have been achieved by screening materials with intrinsically low thermal conductivity [68] using rattling atoms [8–10], liquid-like ions [11,12], and layered structures with strong anharmonicity [13–18].

The density of states near the valence band maximum (VBM) of Cu_2SnSe_3 indicates that its carrier transport properties are dominated by the Cu-Se framework, while the contribution of Sn is weak

* Corresponding author.
** Corresponding author.
E-mail addresses: steve.pennycook@nus.edu.sg (S.J. Pennycook), zhaolidong@buaa.edu.cn (L.-D. Zhao).
[1] Y. Zhou, H. Wu and D. Wang contributed equally to this work.

https://doi.org/10.1016/j.mtphys.2018.11.001
2542-5293/

[19]. Therefore, doping on Sn sites could supply extra carriers through transferring charge to the Cu-Se conducting network, while simultaneously, a high carrier mobility is also expected through retaining the Cu-Se framework. Given these advantages, much work has been performed to substitute Sn sites by Mn [20], Pb [21,22], Ge [23], In [24], and so on. Even though some progress has achieved in the Cu_2SnSe_3 system, the crystal structure of Cu_2SnSe_3 is unclear that is strictly related to the electrical and thermal transport properties. To date, there is no consensus on the crystal structure of Cu_2SnSe_3; various reports can be found, such as cubic [24,25], tetragonal [26], orthorhombic [27], or monoclinic [19,28,29] phases. Moreover, different phases would produce different electrical and thermal transport behaviors [30]. The monoclinic phase is the most widely reported for Cu_2SnSe_3, although its weak superstructure diffractions in X-ray diffraction (XRD) were always ignored and mistaken as a cubic phase [21,31,69]. Additionally, the structure of Cu_2SnSe_3 is also stoichiometrically sensitive. Structural investigations of $Cu_{3-x}Sn_xSe_3$ with x ~1.0 showed that the tetragonal, cubic, and monoclinic phases are controlled by the ratio of Cu and Sn [32]. The tetragonal and cubic phases form under a Cu-rich condition, while the monoclinic phase dominates under an Sn-rich or stoichiometric condition. Interestingly, the heating procedure also has non-negligible impact on the resultant phases. By controlling the annealing and quenching processes, the monoclinic and cubic phases could be formed, as confirmed by XRD Rietveld refinement [30].

In this study, atomically resolved structural imaging is first used to determine the local structure of Cu_2SnSe_3; we report the coexistence of orthorhombic and monoclinic Cu_2SnSe_3 phases through Ag doping on Sn sites and controlling the synthesis process. Compared with the enhanced electrical transport properties via conventionally optimizing carrier concentration, here, we find an unusual three-stage behavior in the temperature-dependent electrical transport properties, which is related to the phase coexistence in the Cu_2SnSe_3 system. Such anomalous electrical transport behavior could be well explained using one proposed band contact model regarding the coexisting nanophases, which are origins of enhanced TE performance of the present Cu_2SnSe_3 system. This work paves the way to enhance TE performance through the design of multiple-phase coexistence in a given TE system.

Experimental section

Raw materials

Reagent chemicals were used as obtained: Cu granules (99.99%, Alfa Aesar, China), Sn granules (99.999%, Aladdin, China), Se chunks (99.99%, Aladdin, China) and Ag rods (99.99%, Trillion Metals, China).

Synthesis

High-purity single elements Cu, Sn, Se, and Ag were weighed according to the nominal compositions of $Cu_2Sn_{1-x}Ag_xSe_3$ (x = 0, 0.01, 0.03, 0.05, 0.07 and 0.09) and then put into fused quartz tubes. The tubes were evacuated to a residual pressure of ~10^{-4} Torr, sealed and slowly heated to 1173 K in 18 h, soaked at this temperature for 10 h, and furnace cooled to 873 K for 24 h, then annealed at 873 K for 1 day. The resultant ingots were crushed into fine powder and then densified by spark plasma sintering (SPS) method (SPS-211LX, Fuji Electronic Industrial Co., Ltd.) at 793 K for 5 min in a 12.7-mm diameter graphite die under an axial compressive stress of 50 MPa in vacuum. Highly dense (>95% of theoretical density) disk-shaped pellets with dimensions of 12.7 mm in diameter and 9 mm in thickness were obtained.

Electrical transport properties

The SPS-densified cylinders were cut into bars with dimensions $9 \times 3 \times 3$ mm^3 that were used for simultaneous measurement of the Seebeck coefficient and the electrical conductivity by CTA (Cryoll, China) instrument under a helium atmosphere from room temperature to 773 K. The samples were coated with a thin (~0.1–0.2 mm) layer of boron nitride to protect the instruments. The uncertainty of the Seebeck coefficient and electrical conductivity measurements is 3%.

Hall measurement

The samples for Hall measurement were polished to a square shape of 6×6 mm^2 with a thickness below 0.5 mm and were contacted by four probes using the van der Pauw method. Hall coefficients (R_H) were measured under a reversible magnetic field of 1.5 T by a Hall measurement system (Lake Shore 8400 Series, Model 8404, USA) at 300–773 K. Carrier density (n_H) was obtained by$n_H = 1/e \cdot R_H$, and carrier mobility (μ_H) was calculated using the relationship $\mu_H = \sigma \cdot R_H$ where σ is the electrical conductivity.

Thermal conductivity

Highly dense cylinders were also cut and polished into squares of 6×6 mm^2 with a thickness of 1–2 mm. The samples were coated with a thin layer of graphite to minimize errors from the emissivity of the material. The thermal conductivity was calculated from $\kappa = D \cdot C_p \cdot \rho$, where the thermal diffusivity coefficient (D) was measured using the laser flash diffusivity method in a laser flash apparatus (Netzsch LFA 457, Germany), the specific heat capacity (C_p) was calculated by the Debye model using a Debye temperature of 148 K, and the density (ρ) was determined using the dimensions and mass of the sample. The uncertainty of the thermal conductivity is estimated to be within 10%. The combined uncertainty for all measurements involved in the calculation of *ZT* is around 20%. Both electrical and thermal properties of samples were measured along the direction perpendicular to the SPS pressing direction.

Electron microscopy and XRD

(Scanning) transmission electron microscopies (STEM and TEM) were used with a JEOL ARM200F equipped with a cold field emission gun and ASCOR probe corrector. The thin TEM specimens were prepared by conventional methods including cutting, grinding, dimpling, polishing, and Ar ion milling on a liquid nitrogen cooling stage. The powder diffraction patterns were obtained with Cu K_α ($\lambda = 1.5418$ Å) radiation in an X-ray powder diffractometer (D/MAX-2500, Rigaku, Japan), operated at 40 kV and 200 mA and equipped with a position-sensitive detector.

UV–Vis–NIR spectroscopy

Optical diffuse reflectance measurements were conducted on the finely ground sample at room temperature. The spectra were recorded in the NIR region (1400–22000 nm) using SHIMADZU IRAffinity-1S spectrophotometer and in the UV–Vis region (350–2600 nm) using SHIMADZU UV-3600 plus spectrophotometer. Absorption (α/S) data were calculated from the reflectance data using the Kubelka–Munk function, $\alpha/S = (1-R)^2/(2R)$. The bandgap was determined by a Tauc plot as the intersection point between the energy axis at the absorption offset and the line extrapolated from the linear portion of the absorption edge in a ($\alpha/S \bullet h\nu$) [2] *vs.* $h\nu$ plot [33].

Density functional theory calculations

First principles density functional theory (DFT) calculations were performed for monoclinic and orthorhombic Cu_2SnSe_3 phases using the full potential linearized augmented plane wave [34] with the augmented plane-wave plus local orbitals (PAW + lo) [35] method, as implemented in the WIEN2k code [36]. The exchange-correlation potentials were treated using the generalized gradient approximation (GGA) of Perdew, Burke, and Ernzerhof (PBE-GGA) [37]. To achieve the energy eigenvalue convergence, the basis function is expanded up to RMT $K_{max} = 8$, where RMT is the minimum radius of muffin-tin spheres and K_{max} is the magnitude of the largest K vector in the plane wave cutoff. We used the muffin-tin spheres (RMT) of radii 2.15 a_0 for Cu, 2.25 a_0 for Sn, and 2.04 a_0 for Se. The Brillouin-zone sampling was checked by the convergence of total energy, until the changes in calculated properties were insignificant. The on-site Coulomb U (U_{eff} = 4 eV) for Cu d electrons was considered in our calculation for accurate description of the band structure [38,39].

Results and discussions

Electrical transport properties

Fig. 1 presents the temperature dependence of electrical transport properties for $Cu_2Sn_{1-x}Ag_xSe_3$ (x = 0–0.09). As shown in Fig. 1a, with an increasing Ag doping fraction, the electrical conductivity of Cu_2SnSe_3 increases dramatically from 46 S cm^{-1} for the undoped sample to 1312 S cm^{-1} for the 7% Ag-doped sample at room temperature. Even a little dopant could enhance the electrical conductivity effectively, e.g., nearly a 10-fold increase after 1% Ag doping. Because Ag^+ could serve as an acceptor dopant, one Ag^+ cation is supposed to provide three holes when located on one Sn^{4+} site. Therefore, such remarkable composition-dependent increase of the electrical conductivity is related to the heavy hole doping. It moves the Fermi level deep into the valence band, yielding a degenerate semiconductor behavior, as shown in the decrease of the electrical conductivity with rising temperature. To estimate the variance of the carrier concentration with Ag doping, room temperature Hall measurements were carried out for the $Cu_2Sn_{1-x}Ag_xSe_3$ samples. The Hall carrier concentration n_H and mobility μ_H are plotted in Fig. 1b. The positive Hall coefficients verify the hole conduction. The highest carrier concentration of 3.71×10^{21} cm^{-3} is obtained in the 3% Ag-doped sample, which is three times larger than that of the 1% Ag-doped sample, revealing that the dopants are completely ionized in both 1% and 3% Ag-doped Cu_2SnSe_3. Further increase of the Ag content does not lead to a further improvement of the carrier concentration, which may be related to the formation of a new phase (discussed later). All doped samples possess ultra-high carrier concentrations > 10^{21} cm^{-3}, which results in an intensive carrier–carrier scattering and leads to a low carrier mobility. Competing carrier concentration and carrier mobility makes the 7% Ag-doped sample possess the highest electrical conductivities of 1312 S cm^{-1} at room temperature and 615 S cm^{-1} at 773 K, which are owing to its moderate carrier mobility (3.9 $cm^2V^{-1}s^{-1}$) and carrier concentration (2.1×10^{21} cm^{-3}).

Remarkably, for samples with Ag dopant greater than or equal to 5%, the electrical conductivities present an unusual three-stage variation: a continuous decline at low temperatures which is linear in the logarithmic σ *vs.* T plot (stage 1), a slower decline and

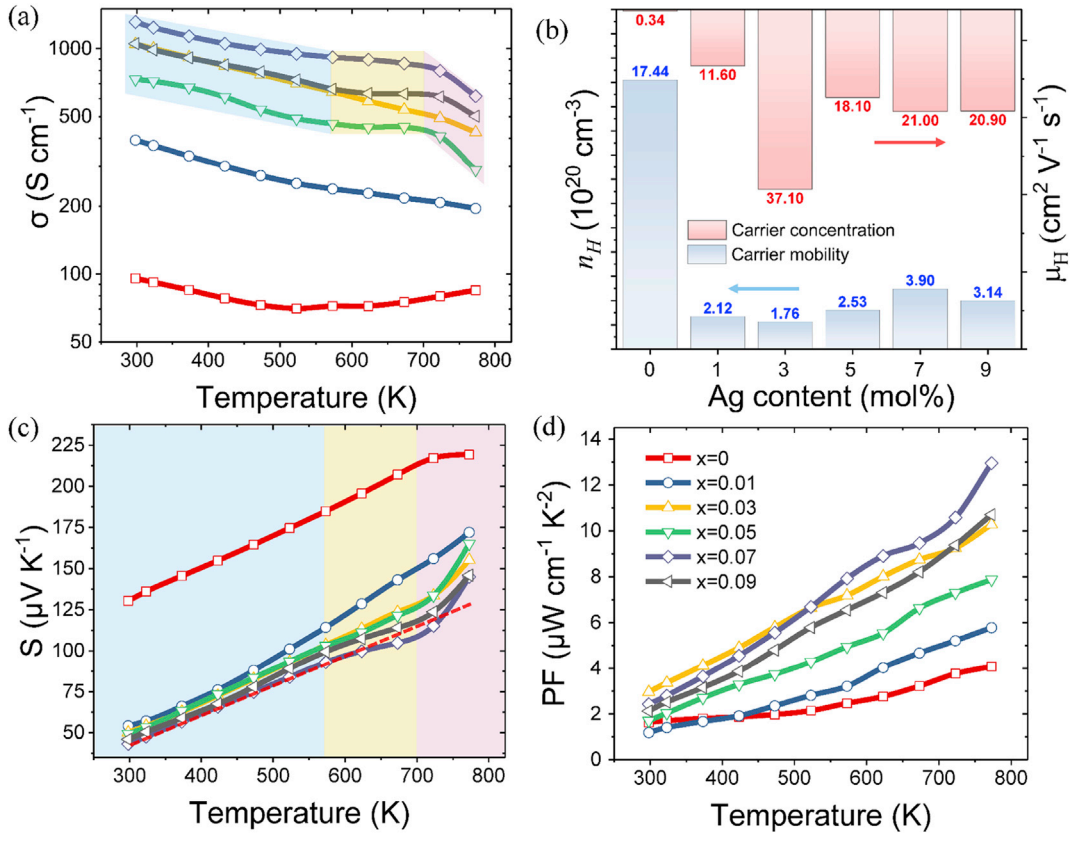

Fig. 1. The temperature dependence of electrical transport properties for $Cu_2Sn_{1-x}Ag_xSe_3$ (x = 0, 0.01, 0.03, 0.05, 0.07, and 0.09): (a) electrical conductivity, (c) Seebeck coefficient, (d) power factor; (b) room temperature Hall carrier concentration and Hall carrier mobility as a function of component.

even a plateau at middle temperatures (stage 2), and finally a sharp deterioration at high temperatures (stage 3). Assuming that the acoustic phonons scattering mechanism is dominated in Cu_2SnSe_3, the Seebeck coefficient for the degenerate semiconductor can be given as the following [40]:

$$S = \frac{8k_B^2\pi^2}{3eh^2}m^*\left(\frac{\pi}{3n}\right)^{\frac{2}{3}}T \quad (1)$$

where k_B, h, m^*, and n are the Boltzmann constant, Planck constant, effective mass, and carrier concentration, respectively. The linear temperature-dependent Seebeck coefficients at temperatures <573 K are consistent with the degenerate semiconductor behavior, as shown in Fig. 1c. Notably, at 573–700 K, Seebeck coefficients exhibit apparent derivations away from the liner trend, which is consistent with the plateau of electrical conductivities at 573–700 K. To investigate the details, we carried out high-temperature Hall measurements for the 7% Ag-doped Cu_2SnSe_3 (Fig. 2). The result illustrates a jump of carriers above 573 K. Specifically, the Seebeck coefficient of $Cu_2Sn_{0.93}Ag_{0.07}Se_3$ reaches +145 μVK^{-1} at 773 K, which is 15 μVK^{-1} larger than the linear extrapolating value (shown as the red dashed line). Fig. 1d illustrates that the PFs of all doped samples are enhanced owing to the optimized carrier concentrations. Moreover, benefitting from the increased carrier concentrations and the sharp increase of Seebeck coefficients at elevated temperatures, the PFs for 5%, 7%, and 9% Ag-doped samples are improved continuously across the whole temperature range. A record high PF of 12.9 $\mu Wcm^{-1}K^{-2}$ is achieved in $Cu_2Sn_{0.93}Ag_{0.07}Se_3$ at 773 K, which increases significantly by ~220% from that of the undoped Cu_2SnSe_3.

To our best knowledge, this three-stage behavior has rarely been observed in Cu_2SnSe_3 doped with Mn [20], Pb [21,22], In [24], and so on. The extra carrier concentrations at high temperatures are mostly ascribed to the temperature-dependent dynamic doping behavior [41] or deep-level impurities [42]. This motivates us to investigate the microstructure of our samples so as to figure out the origin of their improvements in *PFs*.

Crystal structures and phase components

The XRD patterns of all $Cu_2Sn_{1-x}Ag_xSe_3$ specimens are given in Fig. 3. The characteristic peaks of a monoclinic phase are simulated by the pseudo-Voigt method [29]. The monoclinic phase exhibits some low-intensity superstructure peaks between its two most intense peaks at 27.5° and 45°. In the enlarged patterns (Fig. 3b) from 28° to 44°, it is illustrated that the intensities of these superstructure peaks decrease with increasing Ag content; meanwhile, an extra peak at around 31° can be observed in samples with 5% of Ag content or greater. This peak was identified as the CuSe phase (PDF#89-7391) with *P63/mmc* space group [32]. However, in the XRD pattern of CuSe, the (006) reflection at 31° is not the strongest one, while the strongest peak at 28° cannot be observed in Fig. 3b. Moreover, the appearance of CuSe could not fully explain our present results. As shown in Fig. 3c, for samples with the Ag content below 5%, the peaks shift to higher angle; on the contrary, for samples with Ag content beyond 5%, they shift to lower angle. This suggests that the structural evolution is not just atomic substitution in heavily Ag-doped Cu_2SnSe_3 but involves the formation of new phases.

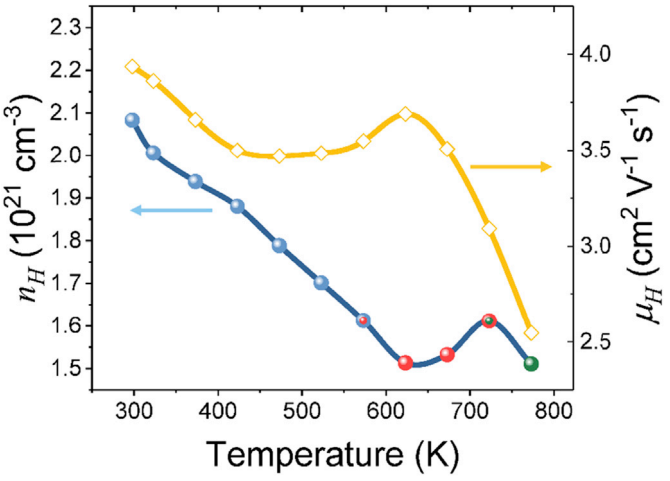

Fig. 2. High-temperature Hall data for $Cu_2Sn_{0.93}Ag_{0.07}Se_3$: Hall carrier concentration and Hall carrier mobility. The blue, red, and green circles denote the stage 1, stage 2, and stage 3, respectively.

To exclude the existence of CuSe, UV–Vis spectroscopy was carried out. The CuSe was reported to possess an indirect bandgap of 1.31 eV and a direct bandgap of 2.2 eV [43]. However, as shown in Fig. 3d, there is no visible absorption at these energies in $Cu_2Sn_{0.93}Ag_{0.07}Se_3$, ruling out the existence of CuSe. Moreover, the three-stage behavior of the temperature-dependent electrical conductivities and Seebeck coefficients suggests another possible existing phase, the orthorhombic Cu_2SnSe_3, which was proposed to possess an order–disorder transition to the cubic phase at around 723 K [44].

As mentioned previously, the crystal structure of Cu_2SnSe_3 is stoichiometrically sensitive, which is related to the nature of the atomic coordination in Cu_2SnSe_3. For the known structures of Cu_2SnSe_3 (monoclinic, cubic, and tetragonal phases), one common characteristic is that all the atoms are tetrahedrally bonded by four atoms with the opposite charge. All these structures can be viewed as variants of the cubic zinc-blende structure, so that Cu_2SnSe_3 can be classified as a diamond-like compound. The main difference among these structures is the arrangement of cations. In the existing reports, the cubic and tetragonal phases were established based on the fractional occupation of Cu and Sn on the same site. These disordered structures are often observed at elevated temperatures in ternary zinc-blende and rock-salt structures, such as $CuInSe_2$ and $AgBiSe_2$ [45,46]. Interestingly, the cubic phase of Cu_2SnSe_3 was also characterized to be a high-temperature phase [19,30]; therefore, the coordinate rule could be applied to obtain the ordered structures for Cu_2SnSe_3. The valence Octet rule was confirmed to play an important role in establishing the energy stable structures in systems of $CuInSe_2$, $AgSbSe_2$, and Cu_2SnS_3 [47]. The Octet rule can be expressed as follow:

$$\frac{\sum_i V_i^+}{CN} + V^- \equiv 8 \quad (2)$$

where the CN, V_i^+, and V^- are the coordination number, the valence electrons of the cations, and anion, respectively. Owing to the eight-electron closed-shell states of the ion, only when the valence electrons in the coordination polyhedron reach eight, will the structure possess the lowest energy. However, different from $CuInSe_2$ and $AgSbSe_2$, which can only meet this rule, the five possible coordination tetrahedra of Cu_2SnSe_3, as shown in Fig. 3e, cannot produce the eight-electron state. Therefore, because the Octet rule cannot be satisfied strictly in one tetrahedron, it indicates two possible structural features for Cu_2SnSe_3: (1) each tetrahedron in Cu_2SnSe_3 structure should possess the smallest deviation to the Octet rule and show an overall average eight-electron state and (2) there exist at least two kinds of tetrahedrons in Cu_2SnSe_3, and the

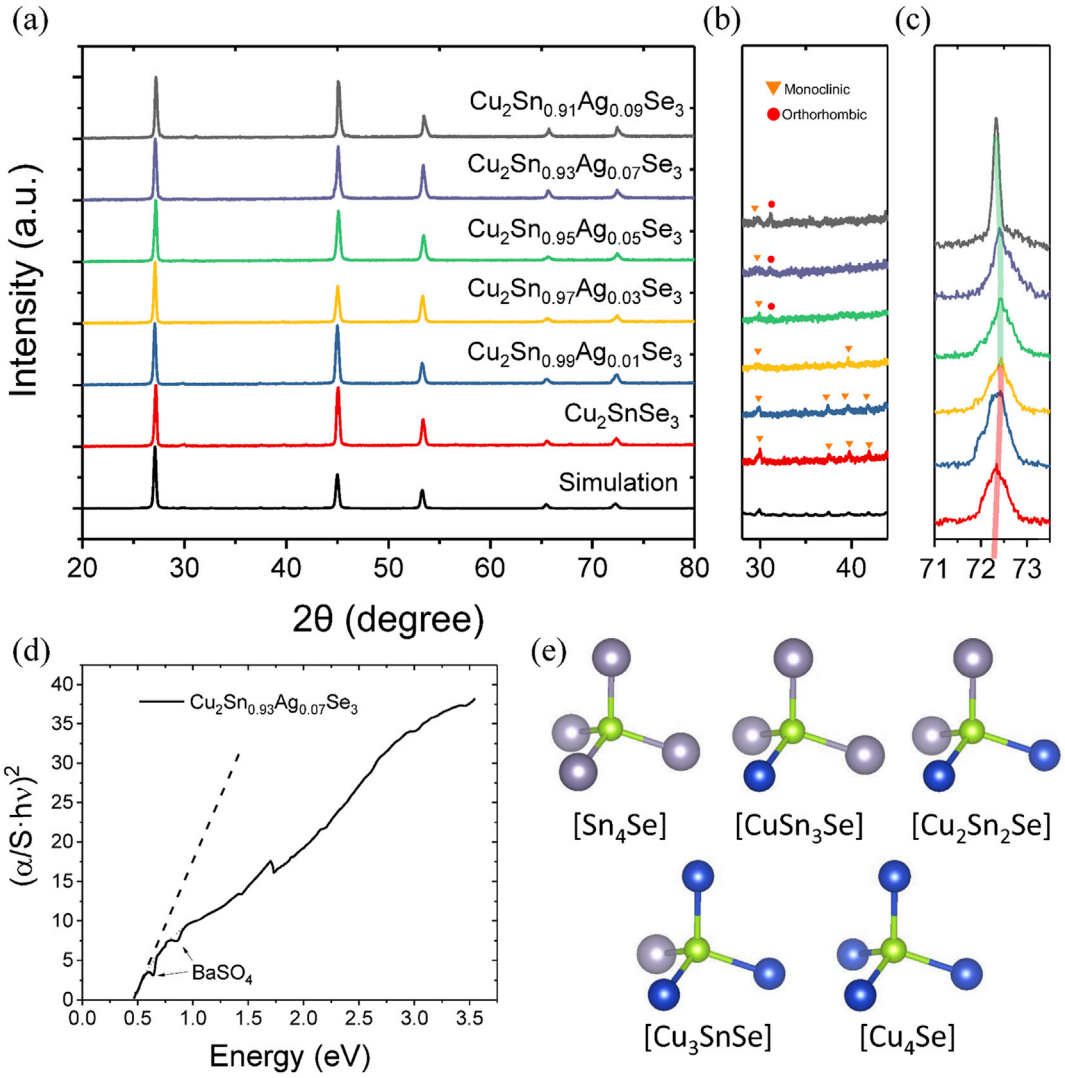

Fig. 3. (a) XRD patterns for $Cu_2Sn_{1-x}Ag_xSe_3$ (x = 0, 0.01, 0.03, 0.05, 0.07, and 0.09), (b) enlarged XRD patterns between 25° and 45°, (c) enlarged XRD patterns between 71° and 73.5°, and (d) Tauc plot for $Cu_2Sn_{0.93}Ag_{0.07}Se_3$ in the UV–Vis region. The inevitable background peaks of $BaSO_4$ are denoted by arrows, (e) possible coordinate tetrahedra for Cu_2SnSe_3. XRD, X-ray diffraction.

degree of off-stoichiometry will cause the different ratios among these coexisting tetrahedrons and thus, results in variations in the total energy. In the stoichiometric Cu_2SnSe_3 with *Cc* symmetry, the ratio of $[Cu_3SnSe]$ to $[Cu_2Sn_2Se]$ tetrahedrons is 2: 1. Based on this proportion, we established several structures for Cu_2SnSe_3 in a $3 \times 3 \times 3$ extended zinc-blende structure and find that the ordered orthorhombic phase, with the space group of *Imm2*, possesses a much lower total energy (−3.60 eV/atom) than that of the monoclinic one (−3.18 eV/atom). This result is consistent with the calculation results on Cu_2SnS_3 [47]. The XRD pattern simulated from the orthorhombic structure can fit the experimental pattern well including the abnormal peak at around 31°.

Microstructure characterizations

To confirm the coexistence for the new orthorhombic phase in the monoclinic matrix, we used TEM/STEM techniques. The TEM image in Fig. 4a shows a twinned structure. The twin variants are not symmetric in width, one having hundreds of nanometers, the other having several nanometers. Within the large variants, there are a high density of stripe-like nanostructures, with length at the microscale and width of several nanometers, as shown in Fig. 4b. Its respective electron diffraction pattern can be indexed as the coexistence of monoclinic and orthorhombic phases, along [010] and [100] zone axes, respectively, as shown in Fig. 4c. These two phases are highly coherent, and all reflections of one phase have their respective coherent ones of the other phase, e.g., 20−2 and 002 planes of monoclinic and 002 and 011 planes of orthorhombic, respectively, with a slight lattice mismatch of ~0.5%. The high-resolution TEM (HRTEM) image in Fig. 4d focuses on one slim variant with the width of ~6 nm in the middle. The HRTEM image in Fig. 4e shows four second-phase orthorhombic stripes within the layered monoclinic matrix, with coherent interfaces along (002) plane of the monoclinic phase or (011) plane of the orthorhombic phase. The coherent phase boundary is also parallel with the twin boundary of the monoclinic matrix. The superstructure reflections of the electron diffraction patterns are from the layered monoclinic phase, as shown in Fig. 4(f1, f2).

Besides the phase coexistence, there are also structural co-existences of different monoclinic and orthorhombic phases. The low-magnification TEM images in Fig. 5(a and b) show stripe-like nanostructures with a similar width of those shown in Fig. 4b but

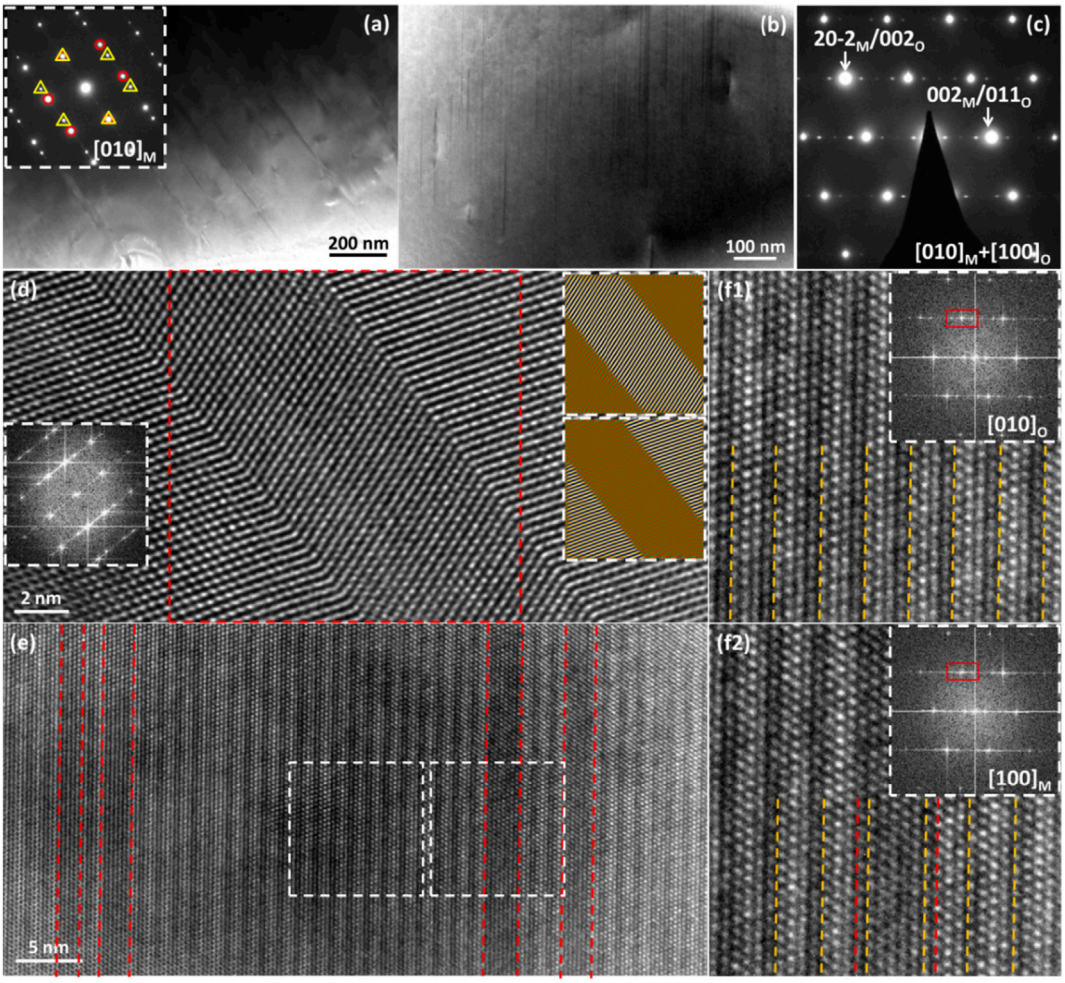

Fig. 4. Phase coexistence of the monoclinic matrix and second-phase orthorhombic Cu_2SnSe_3: (a) low-magnification TEM image showing twins, with its electron diffraction pattern inset; (b) mediate-magnification image showing stripe-like second phases; (c) electron diffraction pattern obtained from (b); (d) HRTEM image of the twin structure; (e) HRTEM image showing four second-phase stripes (orthorhombic phase) within the layered matrix (monoclinic phase); (f1) enlarged image from the layered matrix, with its Fast Fourier Transform (FFT) image inset and (f2) enlarged image around one stripe, with its FFT image inset. FFT, Fast Fourier Transform; TEM, transmission electron microscopy; HRTEM, high-resolution TEM.

with a shorter length of ~200 nm. The electron diffraction pattern in Fig. 5c shows a structural coexistence of two monoclinic phases, M1 (space group *Cc*, a = 6.9670 Å, b = 12.0493 Å, c = 6.9453 Å, $\beta = 109.19°$) [29] and M2 (space group *Cc*, $a = 6.9714$ Å, $b = 12.0787$ Å, $c = 13.3935$ Å, $\beta = 99.865°$) [19,29] along [001] and [100] zone axis, respectively, as shown in Fig. 5(d1, d2), with the sharing 200_{M1}//$00\text{-}4_{M2}$ and (060) planes. Similarly, the electron diffraction pattern in Fig. 5e shows the coexistence of one orthorhombic phase with perpendicular directions along [001] zone axis, as shown in Fig. 5(f1, f2). The HRTEM image in Fig. 6a shows periodically arrayed stripes with width of ~5 nm. The geometric phase analysis (GPA) was performed to obtain the strain distribution [48–50]. The strain analysis presents strain centers along the stripes, as shown in Fig. 6b. Fig. 6c is an HRTEM image showing dense cross-linked stripes, which are two variants of orthorhombic phases. The GPA results in Fig. 6(d1, d2) show strain centers aligning along two directions of the stripes. As the two monoclinic phases are only different in the cation distribution, we used aberration-corrected STEM to observe the structural details of the coexistences of the two monoclinic phases, as shown in Figs. 5c and 6a. STEM high-angle annular dark field (HAADF) produces contrast interpretable by mass-thickness or Z (the number of atoms) contrast [51–53]. Fig. 6e is a STEM-HAADF image covering ordered stripes, which show a different structure from the surrounding matrix. Their difference could be observed clearly in the atomically resolved STEM-HAADF image as shown in Fig. 6(f and g): the brightest Sn-Se chains of the stripes exhibit a zigzag arrangement, which is consistent with M2 phase along [100] zone axis, while those of the matrix possess a rectangular arrangement, which is M1 phase along [001] zone axis. The interface between them is fully coherent, as shown in Fig. 6g. From the previous works that reported the electrical transport properties of the two monoclinic phases [19,24,32], it is found that the M2 phase is more stoichiometric as it possesses higher Seebeck coefficient and lower electrical conductivity, yielding a lower hole concentration. The appearance of these monoclinic phases is attributed to be controlled by the Cu vacancies, which will tune the ratio of the [Cu_3SnSe] to [Cu_2Sn_2Se] tetrahedrons. Furthermore, the high density of various structural and phase coexistences at the nanoscale could service as efficient phonon-scattering centers, without influencing the carrier transport owing to their fully coherent interfaces.

Electronic band structures

To analyze the origin of the unusual enhancement in the electrical transport properties, the band structures of the monoclinic and orthorhombic Cu_2SnSe_3 phases were calculated by DFT. The

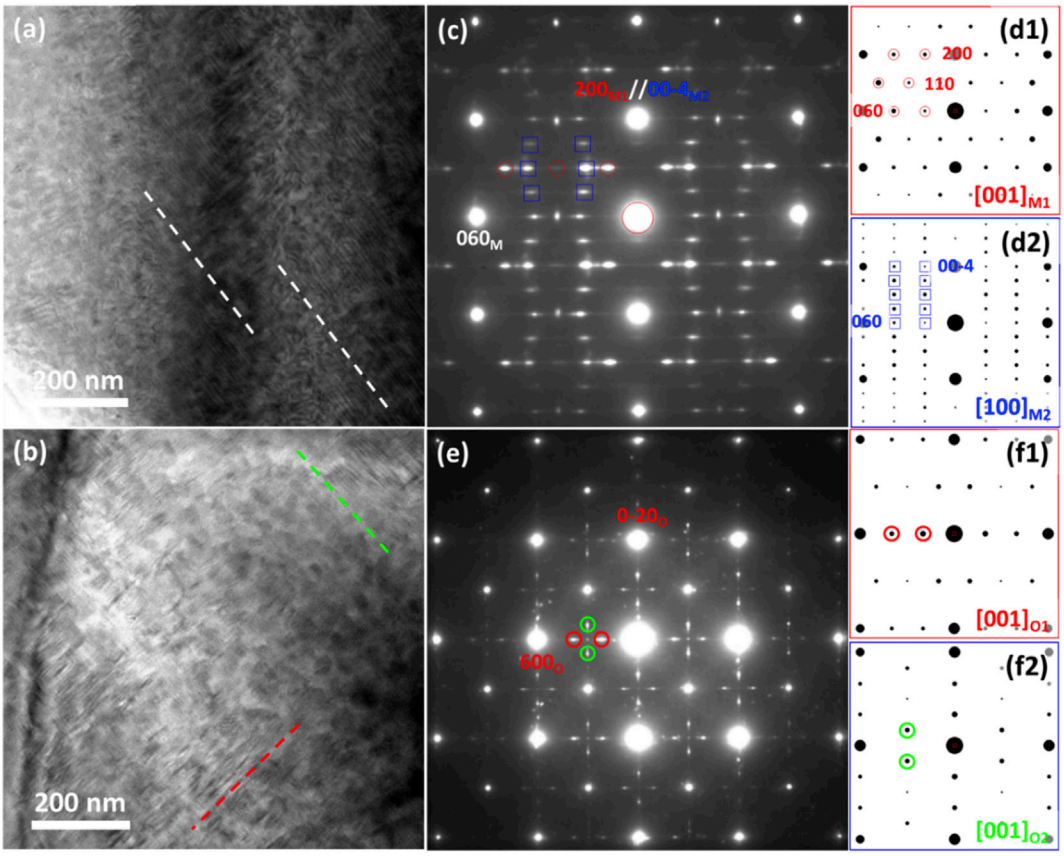

Fig. 5. Structural coexistence of different monoclinic and orthorhombic phases: (a, b) TEM images showing two types of a high density of stripe-like nanostructures; (c) electron diffraction pattern showing the structural coexistence of monoclinic phases along three orientations; (d1, d2) simulated electron diffraction patterns of monoclinic phases along [001] zone axis of M1 phase and [001] zone axis of M2 phase; (e) electron diffraction pattern showing the structural coexistence of orthorhombic phases along two orientations; and (f1, f2) simulated electron diffraction patterns of two monoclinic phases perpendicular along [001] zone axis. TEM, transmission electron microscopy.

band structures shown in Fig. 7a and b illustrate that the monoclinic phase has narrow bandgap near 0.49 eV, while that of the orthorhombic one is slightly smaller. To solve the difficulty originated from the insufficient estimation of the localization of Cu *d* electrons in DFT calculation, we used the PBE + U method in all-electron code WIEN2k to demonstrate the detailed difference in the band structures of the monoclinic and orthorhombic Cu_2SnSe_3 [39]. The VBM for monoclinic phase lie at Γ point, while two valence bands converge and lie 0.06 eV lower than this VBM. Similarly, the orthorhombic phase also has one VBM at Γ point and two more converged bands. The effective mass is $0.85m_e$ and $0.56m_e$ for the monoclinic phase and the orthorhombic phase, respectively. This suggests that the orthorhombic phase is supposed to possess a smaller Seebeck coefficient and a higher carrier mobility when the Fermi level aligns with that of the monoclinic one. The difference between the two monoclinic phases (Fig. 7(c and d)) is negligible, owing to the same space group and similarities in their local structures [47], compared with the obviously different band structures between the orthorhombic (Fig. 7e) and monoclinic phases.

To verify the bandgap by PBE + U method, the optical absorption measurement for Cu_2SnSe_3 was also conducted in a wide energy region of 0.05–3.5 eV among UV–Vis–NIR waveband by two different instruments. As shown in Fig. 7f, the diffuse NIR spectra for Cu_2SnSe_3 are presented as Tauc plots. By extrapolating from the linear portion of the absorption edge, the optical bandgaps for $Cu_2Sn_{1-x}Ag_xSe_3$ (x = 0–0.9) samples show a similar value of 0.46 eV, which is in accord with the calculated bandgap around 0.49 eV in monoclinic Cu_2SnSe_3 phase. It could also be verified by our UV–Vis measurement (Fig. 3d) and the reported spectroscopic ellipsometry measurement [54].

Band contact model for three-stage transport behavior

To further analyze the effects of the orthorhombic phase in the monoclinic matrix, the room temperature Hall carrier mobility μ_H as a function of Hall carrier concentrations n_H is plotted in Fig. 8a. The electrical transport properties can be derived through solving the Boltzmann transport equations. Adopting the single parabolic band (SPB) model, the carrier relaxation time depends on the carrier energy as [55]:

$$\tau = \tau_0 \frac{(r+3/2)}{3/2} \frac{F_{r+1/2}(\eta)}{F_{1/2}(\eta)} = \tau_0 E^r \tag{3}$$

where τ_0 is the energy-independent relaxation time, and r is the scattering parameter. $F_j(\eta)$ is the Fermi integral calculated from the reduced Fermi level, $\eta = E_F/k_BT$:

$$F_j(\eta) = \int_0^\infty \frac{x^j}{e^{(x-\eta)}+1} dx \tag{4}$$

which is determined by the carrier concentration as:

$$n = 4\pi \left(\frac{2m^*kT}{h^2}\right)^{3/2} F_{1/2}(\eta) \tag{5}$$

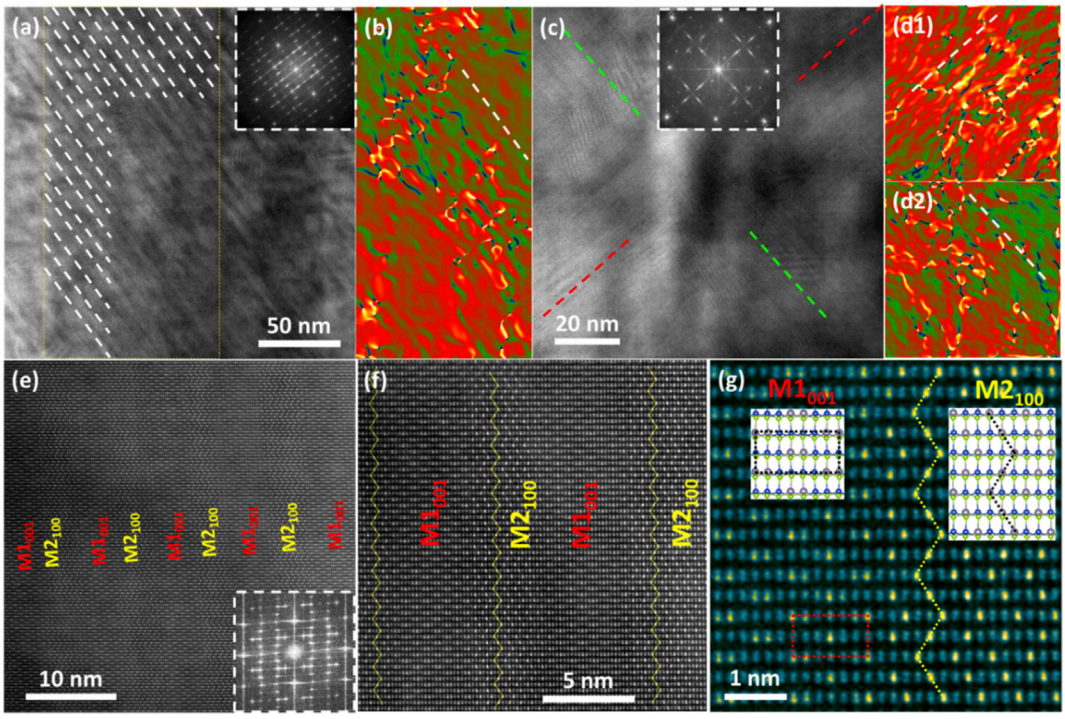

Fig. 6. Structural coexistence of different monoclinic and orthorhombic phases: (a) HRTEM image showing stripe-like monoclinic phases, with its FFT image inset; (b) GPA result of the region marked in (a); (c) HRTEM image showing two perpendicular orthorhombic stripes; (d1, d2) GPA results of (c) along [600] and [0-20] directions; (e) STEM-HAADF image with a large view showing monoclinic stripes along two orientations, with its FFT image inset; (f) atomically resolved STEM-HAADF image; and (g) enlarged STEM-HAADF image focusing on the boundary between two monoclinic stripes. HRTEM, high-resolution transmission electron microscopy; GPA, geometric phase analysis; STEM, scanning transmission electron microscopy; HAADF, high-angle annular dark field.

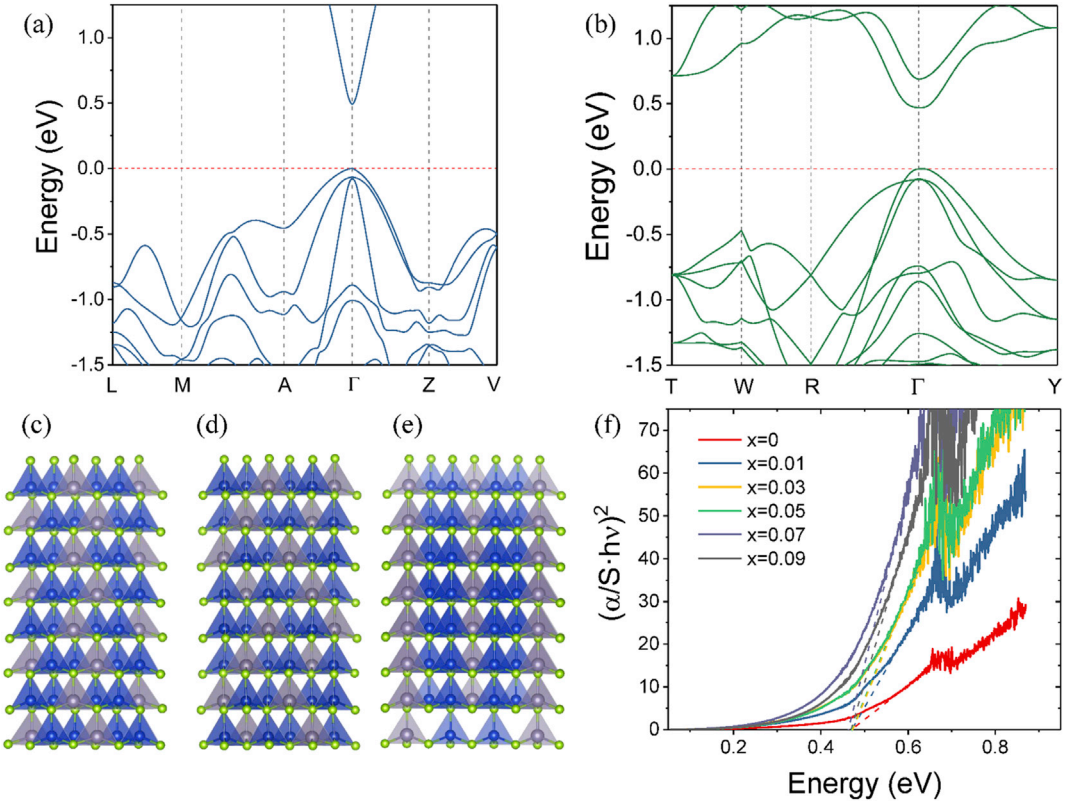

Fig. 7. Band structure for (a) monoclinic-1 Cu_2SnSe_3 and (b) orthorhombic Cu_2SnSe_3; crystal structure for (c) monoclinic-1 Cu_2SnSe_3 (M1), (d) monoclinic-2 Cu_2SnSe_3 (M2), and (e) orthorhombic Cu_2SnSe_3; (f) Tauc plot for $Cu_2Sn_{1-x}Ag_xSe_3$ (x = 0, 0.01, 0.03, 0.05, 0.07, and 0.09) indicating a bandgap of 0.46 eV.

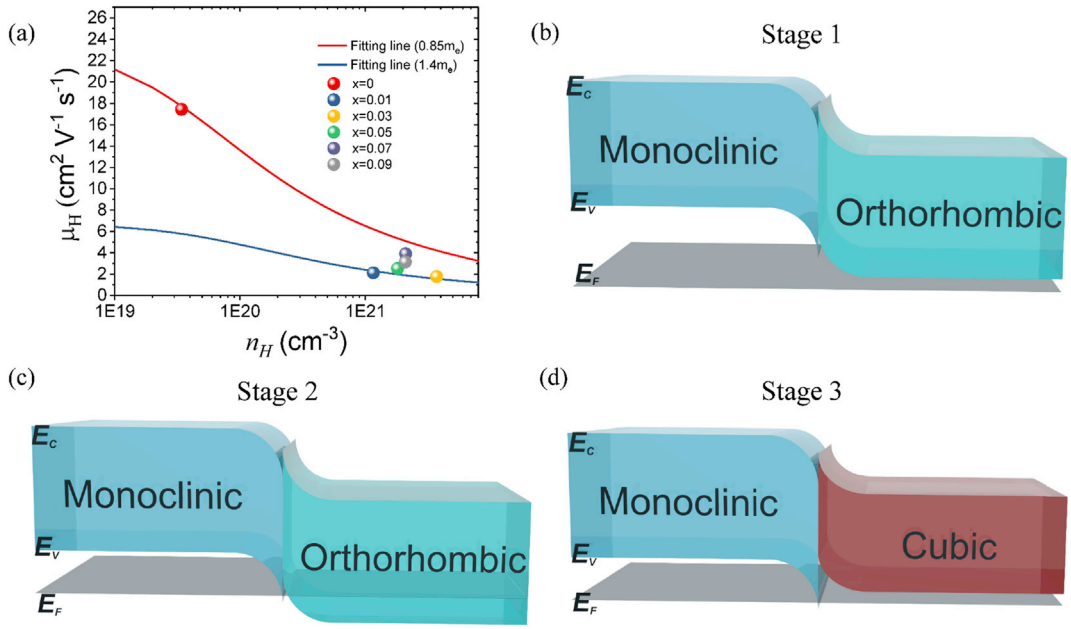

Fig. 8. (a) μ_H *vs.* n_H plot; (b) (c) and (d) are schematics of the band models for Ag-doped Cu_2SnSe_3 with coexistence phases explaining the three-stage behaviors, respectively.

The Hall factor should be considered because the Hall carrier concentration can be expressed as$n_H = n/r_H$, and the Hall factor is also related to the reduced Fermi level:

$$r_H = \frac{3}{2}F_{1/2}(\eta)\frac{F_{-1/2}(\eta)}{2F_0^2(\eta)} \tag{6}$$

While electrons are scattered by acoustic phonon modes, $r = -1/2$. And the carrier relaxation is given by [51]:

$$\tau_0 = \frac{\pi\hbar^4 C_{11}}{\sqrt{2}E_{def}^2(m^* k_B T)^{3/2}} \tag{7}$$

where $C_{11} = 96$ GPa is a component of the elastic tensor derived by DFT calculation, $E_{def} = 21$ eV[31] is the deformation potential which depicts the carrier-scattering strength by acoustic phonons, and m^* is single valley density of states (DOS) effective mass.

Therefore, the relationship between the Hall carrier mobility and the reduced Fermi level can then be obtained by:

$$\mu_H = \frac{e\tau_0}{2m^*}\frac{F_{-1/2}(\eta)}{F_0(\eta)} \tag{8}$$

As shown in Fig. 8a, it is found that the Hall carrier mobility of the undoped Cu_2SnSe_3 is in accord with the fitting line with a calculated DOS effective mass of 0.85m_e. With increasing the Ag doping fraction, the carrier mobility of Cu_2SnSe_3 decreases sharply. Similar behavior is also observed in other works in Cu_2SnSe_3 with large carrier concentration variance [39]. As the carrier concentration increases, the Fermi level is moved into the deep valence band, and the SPB model is deviated [8]. Furthermore, after the appearance of orthorhombic Cu_2SnSe_3 phase, the carrier concentration decreases, while the carrier mobility increases. This variance reveals that the orthorhombic phase has a lower carrier concentration, and the lighter single valence band of orthorhombic phase contributes a higher carrier mobility.

Based on the aforementioned discussion, we propose a phenomenological model to explain the unusual three-stage behavior in Ag-doped Cu_2SnSe_3. As illustrated in the schematic diagrams in Fig. 8(b–d), the coexisting orthorhombic and monoclinic Cu_2SnSe_3 phases could form a p-p heterojunction [56] because they possess different carrier concentrations, which determine different Fermi levels. Once contacting, the Fermi levels of two phases would reach the same level to allow the charge redistribution equilibrium. The bands near the phase boundary are thereby distorted due to the charge transfer. Similar models are observed in rutile and anatase TiO_2 [57,58]. At stage 1, the sharing Fermi level arises toward the VBM with the increasing temperature, resulting in a decrease of the carrier concentration. Such decrease is in accord with the linear decline in the logarithmic coordinated σ *vs.* T plot [59] and the high-temperature Hall carrier concentration variations of $Cu_2Sn_{0.93}Ag_{0.07}Se_3$. At the stage 2, the Fermi level of the orthorhombic phase arises above the valence band. The intrinsic excitation of the orthorhombic phase will offer extra holes, which contributes an increasing effect on the electrical conductivity, opposite to the decreasing effect due to the increasing temperature. It is noteworthy that this excitation in orthorhombic phase will not influence the hole transport natures, both Seebeck and Hall effects, as the electrons are blocked at the interfacial energy barrier of these two phases. Therefore, the coexistence of the metal-like monoclinic phase and the semiconducting orthorhombic phase can lead to a slight reduction and even a plateau for the electrical conductivities at 573–700 K.

At stage 3, owing to the orthorhombic to cubic phase transition, the Fermi level would be overwhelmed by the VBM due to the smaller bandgap of the cubic Cu_2SnSe_3 as illustrated by our bandgap measurement (Fig. 9). Besides the reduction of the carrier concentration, the disordered Cu and Sn cations in the cubic phase also introduce more carrier scattering owing to the randomly distributed cations. The sharp deterioration of the carrier mobility even happens earlier than stage 3, as shown in Fig. 2. Similar behavior is once reported in Zn_4Sb_3 system because of the 'premature effect' of the order–disorder transition [60]. Moreover, owing to the high symmetry of the cubic phase, the Seebeck coefficient is expected to be enhanced as the degeneracy becomes larger [61,62]. This unusual three-stage behavior yields a record high PF in Cu_2SnSe_3-based materials.

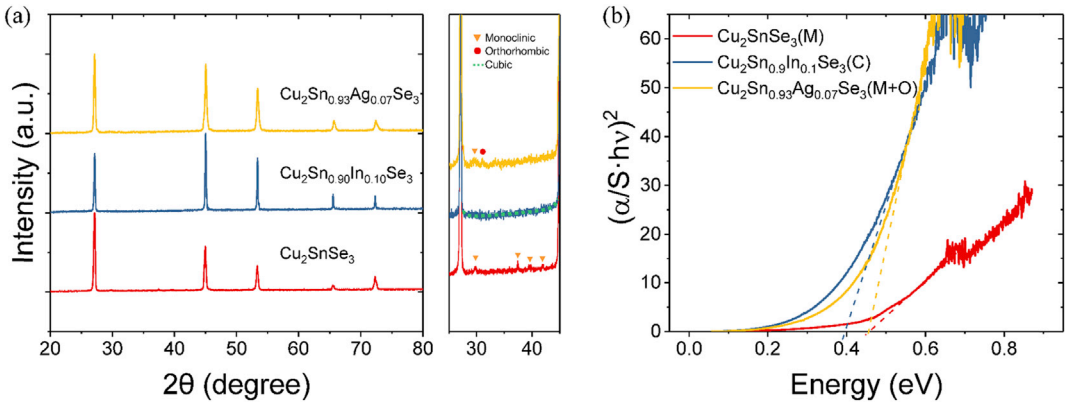

Fig. 9. (a) XRD patterns and enlarged XRD patterns between 25° and 45°, (b) Tauc plot for Ag- and In-doped Cu_2SnSe_3. M, C, and O mark the monoclinic, cubic, and orthorhombic phases, respectively. Owing to the difficulties to obtain the electronic band structures of disordered cubic phase, we synthesized cubic Cu_2SnSe_3 as suggested by previous work [24]. Interestingly, we found that the bandgap of 0.4 eV for cubic Cu_2SnSe_3 is smaller than that of monoclinic phase. XRD, X-ray diffraction.

Thermal transport conductivities and final ZT values

The temperature dependence of total thermal conductivities (κ_{tot}) of $Cu_2Sn_{1-x}Ag_xSe_3$ (x = 0–0.09) is displayed in Fig. 10a. All doped samples possess higher thermal conductivities than the undoped one because of the enhanced electrical conductivities. To exclude the effects of high electrical conductivities, the electronic thermal conductivities (κ_{ele}, Fig. 10b) were calculated through the Wiedemann–Franz law, $\kappa_{ele} = L\sigma T$. The Lorenz number L (Fig. 10c) was extracted based on fitting of the respective Seebeck coefficients, following the SPB model and the acoustic phonon scattering mechanism [63].

As shown in Fig. 10d, the $Cu_2Sn_{0.93}Ag_{0.07}Se_3$ shows the lowest lattice thermal conductivity of 0.85 $Wm^{-1}K^{-1}$ at 723 K, which is ~20% lower than that (1.04 $Wm^{-1}K^{-1}$) of the undoped sample. This reduction appears at high temperatures, which can be attributed to the high density of coexisting nanophases and the disordered Cu and Sn cations inside the nanoscale cubic phases transformed from

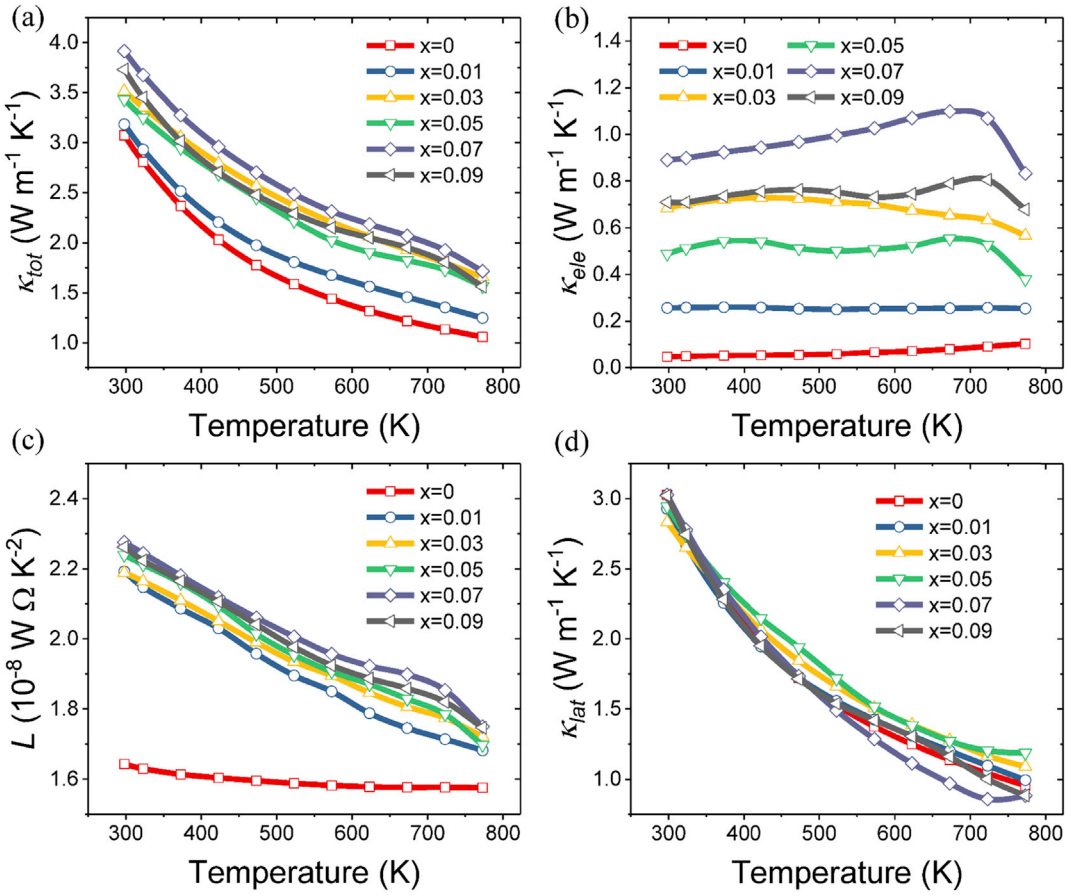

Fig. 10. The temperature dependence of thermal transport properties for $Cu_2Sn_{1-x}Ag_xSe_3$ (x = 0, 0.01, 0.03, 0.05, 0.07, and 0.09): (a) total thermal conductivity, (b) electronic thermal conductivity, (c) Lorenz number, and (d) lattice thermal conductivity.

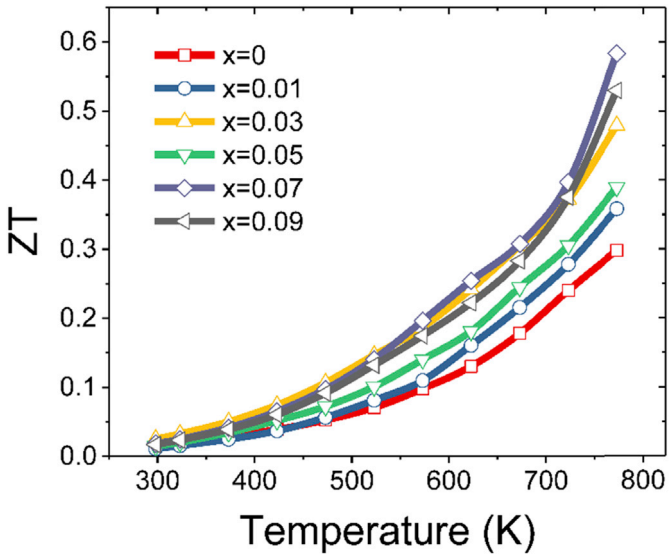

Fig. 11. The thermoelectric figure of merit *ZT* for $Cu_2Sn_{1-x}Ag_xSe_3$ (x = 0, 0.01, 0.03, 0.05, 0.07, and 0.09).

the orthorhombic phases. It is noteworthy that the lattice thermal conductivity of $Cu_2Sn_{0.93}Ag_{0.07}Se_3$ above 723 K shows a slight increase. Owing to the intense variance of the Seebeck coefficient at 773 K, the assumption for fitting the Lorenz number is deviated, which leads to an underestimated electronic thermal conductivity, rather than the bipolar effect. It should also be noted that the total thermal conductivities of our Cu_2SnSe_3-based materials (>1.0 $Wm^{-1}K^{-1}$) are relatively larger than those obtained by non-equilibrium preparation [64], due to the large grain size and the absence of the second phase such as SnSe with a low thermal conductivity, which leaves much room for a further suppression of thermal conductivity of the present system [65,66].

The TE performance (final *ZT* value) is presented in Fig. 11. On account of the optimized carrier concentration, the unusual enhancement of PF through phase coexistence and the effective suppression of the lattice thermal conductivity, the TE performances of the $Cu_2Sn_{1-x}Ag_xSe_3$ (x = 0–0.09) are enhanced. The maximum *ZT* value of 0.6 is achieved in the $Cu_2Sn_{0.93}Ag_{0.07}Se_3$ at 773 K, which is ~100% larger than that of the undoped Cu_2SnSe_3. Therefore, the coexistence of orthorhombic and monoclinic phase produced by Ag doping can effectively promote the TE performance of Cu_2SnSe_3.

Conclusion

To sum up, the introduction of Ag into the Cu_2SnSe_3 can result in the appearance of the nanoscale orthorhombic phase in the monoclinic matrix. The atomically resolved structural images of the Ag-doped Cu_2SnSe_3 directly reveal the coexisting monoclinic and orthorhombic nanophases. The fully coherent interfaces (<0.5% lattice mismatch) between the coexisting phases offer a good structural and band contact between them, hence facilitate the carrier transport. An unusual three-stage behavior is observed in the temperature-dependent electrical transport properties; thus high PFs are achieved in the Ag-doped Cu_2SnSe_3. Benefited from the enhanced PFs and reduced lattice thermal conductivities both caused by the coexisting nanophases, a *ZT* value of 0.6 is achieved in $Cu_2Sn_{0.93}Ag_{0.07}Se_3$ at 773 K, which is double that of the undoped Cu_2SnSe_3. Present results pave the way to enhance TE performance through designing multiple-phase coexistence in a given TE system.

Conflicts of interest

There are no conflicts of interest to declare.

Acknowledgments

This work was supported by the National Key Research and Development Program of China under Grant No. 2018YFB0703600. National Natural Science Foundation of China under grant Nos. 51571007, 51632005 and 51772012, the Beijing Municipal Science and Technology Commission under Grant No. Z171100002017002, the Shenzhen Peacock Plan team under Grant No. KQTD2016022619565911, and 111 Project under Grant No. B17002. S.J.P is grateful to the National University of Singapore for funding. H. W. and S. J. P. would like to acknowledge the support by the Ministry of Education, Singapore, under its Tier 2 Grant (Grant No. MOE2017-T2-1-129).

References

[1] X. Zhang, D.Y. Wang, H.J. Wu, M.J. Yin, Y.L. Pei, S.K. Gong, L. Huang, S.J. Pennycook, J.Q. He, L.D. Zhao, Energy Environ. Sci. 10 (2017) 2420–2431.
[2] Y. Xiao, H. Wu, J. Cui, D. Wang, L. Fu, Y. Zhang, Y. Chen, J. He, S.J. Pennycook, L.-D. Zhao, Energy Environ. Sci. 11 (2018) 2486–2495.
[3] Y. Pei, X. Shi, A. LaLonde, H. Wang, L. Chen, G.J. Snyder, Nature 473 (2011) 66–69.
[4] L.D. Zhao, H.J. Wu, S.Q. Hao, C.I. Wu, X.Y. Zhou, K. Biswas, J.Q. He, T.P. Hogan, C. Uher, C. Wolverton, V.P. Dravid, M.G. Kanatzidis, Energy Environ. Sci. 6 (2013) 3346–3355.
[5] K. Biswas, J. He, I.D. Blum, C.-I. Wu, T.P. Hogan, D.N. Seidman, V.P. Dravid, M.G. Kanatzidis, Nature 489 (2012) 414–418.
[6] L.D. Zhao, X. Zhang, H.J. Wu, G.J. Tan, Y.L. Pei, Y. Xiao, C. Chang, D. Wu, H. Chi, L. Zheng, S.K. Gong, C. Uher, J.Q. He, M.G. Kanatzidis, J. Am. Chem. Soc. 138 (2016) 2366–2373.
[7] J.Q. He, S.N. Girard, J.C. Zheng, L.D. Zhao, M.G. Kanatzidis, V.P. Dravid, Adv. Mater. 24 (2012) 4440–4444.
[8] Y.L. Tang, Z.M. Gibbs, L.A. Agapito, G. Li, H.S. Kim, M.B. Nardelli, S. Curtarolo, G.J. Snyder, Nat. Mater. 14 (2015) 1223–1228.
[9] X.Y. Zhou, G.Y. Wang, L. Zhang, H. Chi, X.L. Su, J. Sakamoto, C. Uher, J. Mater. Chem. 22 (2012) 2958–2964.
[10] W.S. Liu, B.P. Zhang, J.F. Li, L.D. Zhao, J. Phys. D Appl. Phys. 40 (2007) 6784–6790.
[11] H.L. Liu, X. Shi, F.F. Xu, L.L. Zhang, W.Q. Zhang, L.D. Chen, Q. Li, C. Uher, T. Day, G.J. Snyder, Nat. Mater. 11 (2012) 422–425.
[12] R. Nunna, P.F. Qiu, M.J. Yin, H.Y. Chen, R. Hanus, Q.F. Song, T.S. Zhang, M.Y. Chou, M.T. Agne, J.Q. He, G.J. Snyder, X. Shi, L.D. Chen, Energy Environ. Sci. 10 (2017) 1928–1935.
[13] L.-D. Zhao, S.-H. Lo, Y. Zhang, H. Sun, G. Tan, C. Uher, C. Wolverton, V.P. Dravid, M.G. Kanatzidis, Nature 508 (2014) 373–377.
[14] L.D. Zhao, G.J. Tan, S.Q. Hao, J.Q. He, Y.L. Pei, H. Chi, H. Wang, S.K. Gong, H.B. Xu, V.P. Dravid, C. Uher, G.J. Snyder, C. Wolverton, M.G. Kanatzidis, Science 351 (2016) 141–144.
[15] W.K. He, D.Y. Wang, J.F. Dong, Y. Qiu, L.W. Fu, Y. Feng, Y.J. Hao, G.T. Wang, J.F. Wang, C. Liu, J.F. Li, J.Q. He, L.D. Zhao, J. Mater. Chem. A 6 (2018) 10048–10056.
[16] C. Chang, M.H. Wu, D.S. He, Y.L. Pei, C.F. Wu, X.F. Wu, H.L. Yu, F.Y. Zhu, K.D. Wang, Y. Chen, L. Huang, J.F. Li, J.Q. He, L.D. Zhao, Science 360 (2018) 778–782.
[17] Y.M. Zhou, L.D. Zhao, Adv. Mater. 29 (2017) 14.
[18] G.D. Tang, W. Wei, J. Zhang, Y.S. Li, X. Wang, G.Z. Xu, C. Chang, Z.H. Wang, Y.W. Du, L.D. Zhao, J. Am. Chem. Soc. 138 (2016) 13647–13654.
[19] J. Fan, W. Carrillo-Cabrera, L. Akselrud, I. Antonyshyn, L. Chen, Y. Grin, Inorg. Chem. 52 (2013) 11067–11074.
[20] X. Lu, D.T. Morelli, J. Electron. Mater. 41 (2012) 1554–1558.
[21] K.S. Prasad, A. Rao, K. Tyagi, N.S. Chauhan, B. Gahtori, S. Bathula, A. Dhar, Physica B 512 (2017) 39–44.
[22] S.K. Prasad, A. Rao, B. Gahtori, S. Bathula, A. Dhar, C.-C. Chang, Y.-K. Kuo, Physica B 520 (2017) 7–12.
[23] E.J. Skoug, J.D. Cain, D.T. Morelli, J. Alloy. Comp. 506 (2010) 18–21.
[24] X. Shi, L. Xi, J. Fan, W. Zhang, L. Chen, Chem. Mater. 22 (2010) 6029–6031.
[25] G.S. Babu, Y.B.K. Kumar, Y.B.K. Reddy, V.S. Raja, Mater. Chem. Phys. 96 (2006) 442–446.
[26] J. Fan, W. Carrillo-Cabrera, I. Antonyshyn, Y. Prots, I. Veremchuk, W. Schnelle, C. Drathen, L.D. Chen, Y. Grin, Chem. Mater. 26 (2014) 5244–5251.
[27] J. Rivet, J. Flahaut, T. Laruelle, Compt. Rend. Acad. Sci. Paris 257 (1963) 161–164.
[28] L. Gulay, M. Daszkiewicz, T. Ostapyuk, O. Klymovych, O. Zmiy, Acta Crystallogr. Sect. C Cryst. Struct. Commun. 66 (2010) i58–i60.

[29] G. Delgado, A. Mora, G. Marcano, C. Rincón, Mater. Res. Bull. 38 (2003) 1949–1955.
[30] M. Siyar, J.Y. Cho, Y. Youn, S. Han, M. Kim, S.H. Bae, C. Park, J. Mater. Chem. C 6 (2018) 1780–1788.
[31] G. Marcano, C. Rincon, L.M. de Chalbaud, D.B. Bracho, G.S. Perez, J. Appl. Phys. 90 (2001) 1847–1853.
[32] J. Fan, W. Schnelle, I. Antonyshyn, I. Veremchuk, W. Carrillo-Cabrera, X. Shi, Y. Grin, L. Chen, Dalton Trans. 43 (2014) 16788–16794.
[33] Z.M. Gibbs, A. LaLonde, G.J. Snyder, New J. Phys. 15 (2013) 18.
[34] P.E. Blöchl, Phys. Rev. B 50 (1994) 17953–17979.
[35] E. Sjöstedt, L. Nordström, D.J. Singh, Solid State Commun. 114 (2000) 15–20.
[36] K. Schwarz, P. Blaha, G.K.H. Madsen, Comput. Phys. Commun. 147 (2002) 71–76.
[37] J.P. Perdew, K. Burke, M. Ernzerhof, Phys. Rev. Lett. 77 (1996) 3865–3868.
[38] Y.B. Zhang, J.W. Zhang, W.W. Gao, T.A. Abtew, Y.W. Wang, P.H. Zhang, W.Q. Zhang, J. Chem. Phys. 139 (2013) 7.
[39] L. Xi, Y.B. Zhang, X.Y. Shi, J. Yang, X. Shi, L.D. Chen, W. Zhang, J. Yang, D.J. Singh, Phys. Rev. B 86 (2012).
[40] G. Tan, L.-D. Zhao, M.G. Kanatzidis, Chem. Rev. 116 (2016) 12123–12149.
[41] L. You, Y. Liu, X. Li, P. Nan, B. Ge, Y. Jiang, P. Luo, S. Pan, Y. Pei, W. Zhang, G.J. Snyder, J. Yang, J. Zhang, J. Luo, Energy Environ. Sci. 11 (2018) 1848–1858.
[42] Q. Zhang, Q. Song, X. Wang, J. Sun, Q. Zhu, K. Dahal, X. Lin, F. Cao, J. Zhou, S. Chen, G. Chen, J. Mao, Z. Ren, Energy Environ. Sci. 11 (2018) 933–940.
[43] H.-L. Li, Y.-C. Zhu, S. Avivi, O. Palchik, J.-p. Xiong, Y. Koltypin, V. Palchik, A. Gedanken, J. Mater. Chem. 12 (2002) 3723–3727.
[44] J. Rivet, Ann. Chim. 10 (1965) 243–270.
[45] M.M. Zou, Q. Liu, C.F. Wu, T.R. Wei, Q. Tan, J.F. Li, F. Chen, RSC Adv. 8 (2018) 7055–7061.
[46] S. Schorr, G. Geandier, Cryst. Res. Technol. 41 (2006) 450–457.
[47] Y.-T. Zhai, S. Chen, J.-H. Yang, H.-J. Xiang, X.-G. Gong, A. Walsh, J. Kang, S.-H. Wei, Phys. Rev. B 84 (2011), 075213.
[48] H.J. Wu, F.S. Zheng, D. Wu, Z.H. Ge, X.Y. Liu, J.Q. He, Nano Energy 13 (2015) 626–650.
[49] H.J. Wu, J. Carrete, Z.Y. Zhang, Y.Q. Qu, X.T. Shen, Z. Wang, L.D. Zhao, J.Q. He, NPG Asia Mater. 6 (2014) 11.
[50] J.Q. He, I.D. Blum, H.Q. Wang, S.N. Girard, J. Doak, L.D. Zhao, J.C. Zheng, G. Casillas, C. Wolverton, M. Jose-Yacaman, D.N. Seidman, M.G. Kanatzidis, V.P. Dravid, Nano Lett. 12 (2012) 5979–5984.
[51] Y. Xiao, H.J. Wu, W. Li, M.J. Yin, Y.L. Pei, Y. Zhang, L.W. Fu, Y.X. Chen, S.J. Pennycook, L. Huang, J. He, L.D. Zhao, J. Am. Chem. Soc. 139 (2017) 18732–18738.
[52] H.J. Wu, C. Chang, D. Feng, Y. Xiao, X. Zhang, Y.L. Pei, L. Zheng, D. Wu, S.K. Gong, Y. Chen, J.Q. He, M.G. Kanatzidis, L.D. Zhao, Energy Environ. Sci. 8 (2015) 3298–3312.
[53] S.J. Pennycook, L.A. Boatner, Nature 336 (1988) 565.
[54] S. Choi, J. Kang, J. Li, H. Haneef, N. Podraza, C. Beall, S.-H. Wei, S. Christensen, I. Repins, Appl. Phys. Lett. 106 (2015), 043902.
[55] Z. Feng, T. Jia, J. Zhang, Y. Wang, Y. Zhang, Phys. Rev. B 96 (2017) 235205.
[56] R.C. Kumar, Solid State Electron. 11 (1968) 543–551.
[57] D.O. Scanlon, C.W. Dunnill, J. Buckeridge, S.A. Shevlin, A.J. Logsdail, S.M. Woodley, C.R.A. Catlow, M.J. Powell, R.G. Palgrave, I.P. Parkin, G.W. Watson, T.W. Keal, P. Sherwood, A. Walsh, A.A. Sokol, Nat. Mater. 12 (2013) 798.
[58] P. Deák, B. Aradi, T. Frauenheim, J. Phys. Chem. C 115 (2011) 3443–3446.
[59] K. Peng, X. Lu, H. Zhan, S. Hui, X. Tang, G. Wang, J. Dai, C. Uher, G. Wang, X. Zhou, Energy Environ. Sci. 9 (2016) 454–460.
[60] S. Bhattacharya, R.P. Hermann, V. Keppens, T.M. Tritt, G.J. Snyder, Phys. Rev. B 74 (2006) 134108.
[61] R.H. Liu, H.Y. Chen, K.P. Zhao, Y.T. Qin, B.B. Jiang, T.S. Zhang, G. Sha, X. Shi, C. Uher, W.Q. Zhang, L.D. Chen, Adv. Mater. 29 (2017) 7.
[62] J.W. Zhang, R.H. Liu, N.A. Cheng, Y.B. Zhang, J.H. Yang, C. Uher, X. Shi, L.D. Chen, W.Q. Zhang, Adv. Mater. 26 (2014) 3848–3853.
[63] L.-D. Zhao, S.-H. Lo, J. He, H. Li, K. Biswas, J. Androulakis, C.-I. Wu, T.P. Hogan, D.-Y. Chung, V.P. Dravid, M.G. Kanatzidis, J. Am. Chem. Soc. 133 (2011) 20476–20487.
[64] Y. Li, G. Liu, J. Li, K. Chen, L. Li, Y. Han, M. Zhou, M. Xia, X. Jiang, Z. Lin, New J. Chem. 40 (2016) 5394–5400.
[65] G. Liu, K. Chen, J. Li, Y. Li, M. Zhou, L. Li, J. Eur. Ceram. Soc. 36 (2016) 1407–1415.
[66] Y. Li, G. Liu, T. Cao, L. Liu, J. Li, K. Chen, L. Li, Y. Han, M. Zhou, Adv. Funct. Mater. 26 (2016) 6025–6032.
[67] X. Tan, H. Wang, G. Liu, J.G. Noudem, H. Hu, J. Xu, H. Shao, J. Jiang, Mater. Today Phys. 7 (2018) 35–44.
[68] C. Chang, L.-D. Zhao, Mater. Today Phys. 4 (2018) 50–57.
[69] W. Xu, Y. Liu, A. Marcelli, P.P. Shang, W.S. Liu, Mater. Today Phys. 6 (2018) 68–82.